A directional coupler for partial discharge measurements in gas-insulated substations

Mier, Christian; Rodrigo Mor, Armando; Vaessen, Peter

DOI
10.1016/j.measurement.2023.113996

Publication date
2024

Document Version
Final published version

Published in
Measurement: Journal of the International Measurement Confederation

Measurement 225 (2024) 113996

Contents lists available at ScienceDirect

Measurement

journal homepage: www.elsevier.com/locate/measurement

A directional coupler for partial discharge measurements in gas-insulated substations

Christian Mier [a,*], Armando Rodrigo Mor [b], Peter Vaessen [a]

[a] Delft University of Technology, High Voltage Technology Group, Mekelweg 4, 2628 CD Delft, Netherlands
[b] Universitat Politècnica de València, Instituto de Tecnología Eléctrica, Camino de Vera s/n, 46022 Valencia, Spain

ARTICLE INFO

Keywords:
Partial discharges
PD sensors
Gas-insulated
Calibration
Directional coupler

ABSTRACT

This paper introduces a directional coupler for partial discharge (PD) measurements in gas-insulated substations (GIS). The sensor comprises a combination of magnetic and electric couplers, effectively segregating forward and backward pulses to enhance PD charge estimation and defect location. The sensor's design was supported with finite element method simulations and measurements conducted in a transverse electromagnetic test bench. Comparative analyses were performed against independent magnetic and electric couplers. The charge estimation and the directional coupler's directivity were evaluated in both the test bench and a full-scale GIS with different PD defects. Initially, the combined magnetic and the electric couplers exhibited undesired interactions, prompting corrective measures. Subsequent adjustments included changes to the electric coupler material and modifications to the magnetic coupler construction. The resulting high-voltage directional coupler performed better than the separated couplers in a GIS with discontinuities. This partial discharge sensor emerges as a candidate for future SF_6-free alternative GIS.

1. Introduction

Partial discharge (PD) measurement is a widely recognised technique for diagnosing electric insulation and is often required for routine and site tests. The PD charge magnitude quantifies the insulation degradation level in pC and allows different measuring systems to be calibrated to a common reference value [1]. The IEC 60270 [2] is the only standard for PD charge measurements in gas-insulated substations (GIS). However, its accuracy is compromised by the GIS length, and its implementation is impractical for online monitoring. The ultra-high frequency (UHF) method has been widely used, but in some cases, its frequency range exceeds the PD bandwidth in SF6-alternatives gases [3]. Moreover, the PD charge cannot be accurately estimated in the UHF range [4].

In previous research [5], the authors presented a novel GIS PD magnetic sensor capable of measuring the PD charge. This sensor consists of a loop installed in the same mounting hole as the commercial UHF sensor. Moreover, in [6], the authors showed that an electric coupler can also capture the PD charge when it is limited to the very-high frequency (VHF) range. Fig. 1 a) illustrates the operation of the electric and magnetic sensors on the left and right GIS mounting holes, respectively. When the PD pulse propagates through the GIS, the magnetic sensor picks up the magnetic field (green arrows) produced by the enclosure current (blue arrows). Simultaneously, the electric sensor couples the electric field (red arrows) produced by the pulse wave. Therefore, the magnetic and electric sensors operate by coupling the PD magnetic and electric fields, respectively.

The electromagnetic fields coupled to the sensors, depicted in Fig. 1 a), represent the propagation in the transverse electromagnetic (TEM) mode. This propagation mode covers the very-high frequency range, where the PD charge information is contained [7]. The electric and magnetic sensors can be modelled in the VHF range using the circuits in Fig. 1 b) and c), resulting in (1) and (2), in accordance to [6,8,9]. In these models, $\boldsymbol{I}_{pd}$ represents the PD current, Z_{GIS} is the local GIS characteristic impedance, M and C_1 are the mutual inductance and capacitance between the GIS and the sensors, L is the sensors' self-inductance, C_2 and C_m are the sensors' capacitance to ground, R is the load, and $\boldsymbol{V}_o$ is the sensors' output voltage. These models are valid for the PD charge

Abbreviations: PD, partial discharge; GIS, gas-insulated substation; UHF, ultra-high frequency; VHF, very-high frequency; TEM, transverse electromagnetic mode; DGISC, directional GIS coupler; CB, carbon black epoxy resin mixture; V2I, voltage double integral; LPF, low-pass filter; JP, jumping particle; SD, surface discharge; HFCT, high-frequency current transformer.

* Corresponding author.
E-mail address: c.mierescurra@tudelft.nl (C. Mier).

https://doi.org/10.1016/j.measurement.2023.113996
Received 20 July 2023; Received in revised form 15 November 2023; Accepted 4 December 2023
Available online 7 December 2023

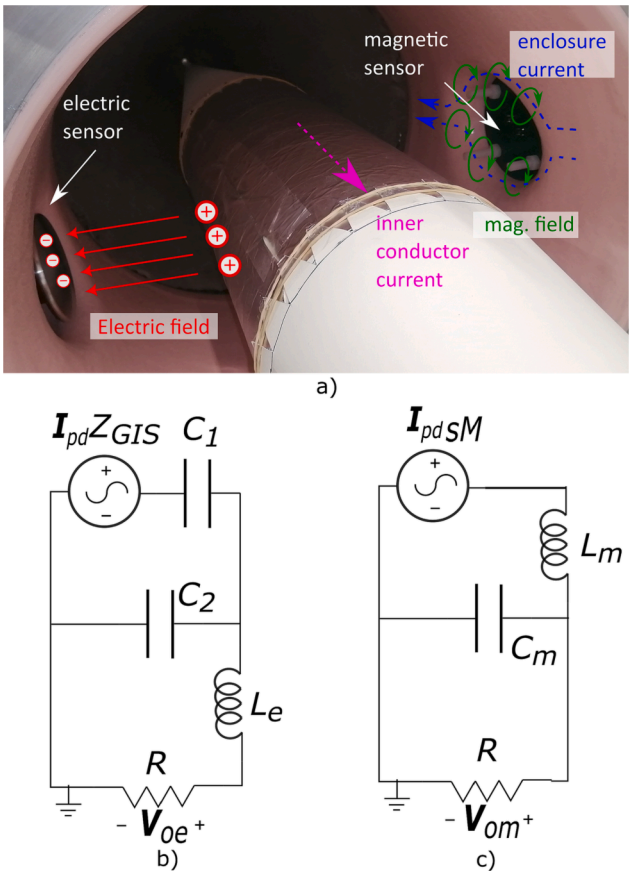

Fig. 1. A) illustration of the electric (left) and magnetic (right) sensors in the GIS, showing the inner conductor current (pink arrow), the enclosure current (blue arrows), the mounting hole's magnetic field (green arrows), and the charges induced in the electric coupler (red dots). electric b) and magnetic c) sensors' circuits.

estimation [10]. It is worth mentioning that for the PD charge estimation in GIS, the discontinuities produced by circuit breakers, voltage and current transformers, T-branches, disconnector switches, earthing switch, etc., produce PD pulse overlapping [11], affecting the PD charge estimation [1].

$$\frac{\boldsymbol{V}_{oe}(s)}{\boldsymbol{I}_{pd}(s)} \approx \frac{\overbrace{sRZ_{GIS}C_1}^{k_e}}{s^2\underbrace{L_eC_2}_{1/\omega_{2e}^2} + s\underbrace{C_2R}_{1/\omega_{1e}} + 1} \tag{1}$$

$$\frac{\boldsymbol{V}_{om}(s)}{\boldsymbol{I}_{pd}(s)} \approx \frac{\overbrace{s\,M}^{k_m}}{s^2\underbrace{L_mC_m}_{1/\omega_{2m}^2} + s\underbrace{L_m/R}_{1/\omega_{1m}} + 1} \tag{2}$$

In [12], the authors developed the so-called "synergy" method that identifies the forward and backward components of the PD. In this method, the sensors were installed in the same transversal position within the GIS but in adjacent mounting holes, as depicted in Fig. 1. Using the signals measured by both sensors, the synergy processing of the electric and magnetic measurements eliminates the backward component. This results in the calculation of the incident pulse, enhancing the PD charge estimation when PD pulses overlap due to pulse reflections within the GIS. However, this method requires both sensors' signals to arrive simultaneously, which represents an additional challenge to the synergy method. This digitally processed synergy method is identified in this paper as "software synergy.".

This paper proposes a "hardware synergy" method by physically combining the electric and magnetic couplers in a manner similar to a directional coupler. The combination of both couplers, identified in this paper as directional GIS coupler (DGISC), offers advantages over the previous method, including power-frequency voltage shielding, single mounting hole installation, and incident and reflected pulses segregation without the need for additional software signal processing. However, the physical combination of both sensors requires additional considerations in terms of the sensor design and the calibration procedure.

This article begins by introducing directional couplers theory and its relation to the proposed sensor. In the second part, the interaction between the electric and magnetic couplers is analysed through finite element simulation and tested in a TEM test bench. The goal of this section is not to present an optimised sensor design, but rather to highlight the impact of physical phenomena on the design parameters. Subsequently, the DGISC design and its calibration are presented. Finally, the sensor's response and charge estimation capabilities are tested in the TEM test bench and a full-scale GIS.

2. The directional coupler

Directional couplers are widely used for radio frequency applications. Their primary function is to measure incident and reflected waves, and they are used to check the connection integrity of antennas and vector network analysers [13]. Fig. 2 shows the fundamentals of the directional coupler. In Fig. 2 a), a wave travels in the main circuit (top line) from left to right, with its current (blue arrow) in the same direction. This wave produces an electric field (red arrows) and a magnetic field (green cross) in the secondary circuit (bottom circuit), where the electric field induces a common-mode current (light-red arrows) and the magnetic field a counterclockwise current (light-blue arrows). These induced electric and magnetic currents are added in the left resistor and subtracted in the right one. Now, if the secondary circuit is designed to couple the same amount of inductive and capacitive current, the induced voltage is doubled and nulled in the left and right loads, respectively. In Fig. 2 b), the wave travels from right to left, inducing an electric field in the same direction as in the previous case but with an opposite polarity magnetic field. This results in a doubled and a nulled voltage in the right and left loads, respectively. Therefore, this configuration measures the forward component in one load and the backward component in the other. The directional coupler's ability to separate the forward and backward wave propagation is quantified by the directivity.

The GIS PD electric and magnetic sensors can be configured similarly to the directional coupler. In this case, the GIS acts as the primary circuit, and the sensors function as the couplers of the secondary circuit. A notable distinction between a traditional directional coupler and the DGISC lies in the high voltage associated with the latter. This imposes limitations on the sensor's positioning and geometry, requiring it to be adapted to the GIS mounting hole and to cope with the electric field at the power frequency, typically 50/60 Hz or DC.

The sensors depicted in Fig. 1 can be interconnected to simultaneously couple the PD electric and magnetic fields, as illustrated in Fig. 3 a). The integration of both sensors into a single circuit leads to the electric model depicted in Fig. 3 b). In this representation, the lower

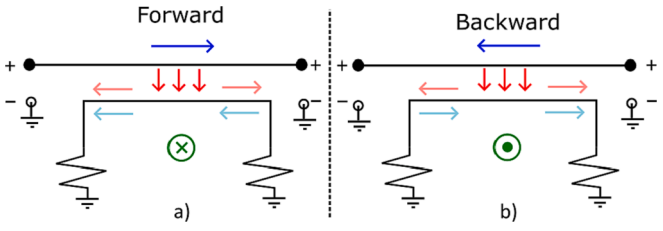

Fig. 2. A) forward and b) backward components induced in a directional coupler.

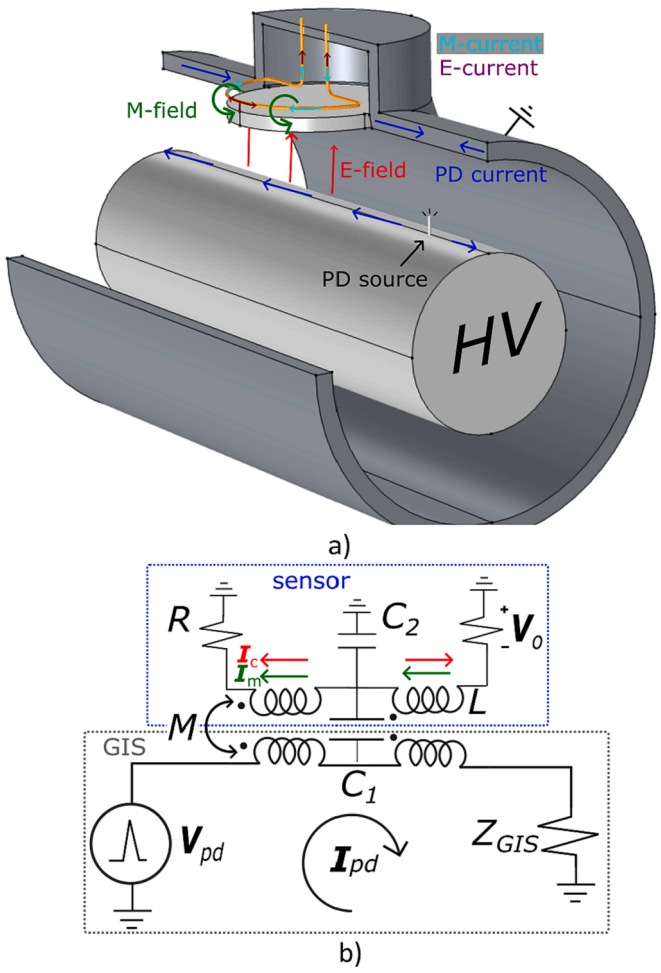

Fig. 3. DGISC a) induced forward and backward components illustration and b) electric circuit.

circuit corresponds to the GIS, while the upper one corresponds to the sensor. The DGISC model (3) results in the superposition of the electric (1) and magnetic (2) sensors' transfer functions. The addition or subtraction between the magnetic and electric components depends upon the propagation direction, as with the directional coupler.

$$\frac{\boldsymbol{V}_{oe}+\boldsymbol{V}_{om}}{\boldsymbol{I}_{pd}}=\frac{\boldsymbol{V}_{o}}{\boldsymbol{I}_{pd}}\approx\underbrace{\frac{sk_e}{s^2/\omega_{2e}^2+s/\omega_{1e}+1}}_{electric-component}\pm\underbrace{\frac{sk_m}{s^2/\omega_{2m}^2+s/\omega_{1m}+1}}_{magnetic-component} \tag{3}$$

The DGISC measures both the forward and backward components of a PD, providing advantages over using a single magnetic or electric sensor. This integrated approach enhances the PD charge estimation, facilitates the PD defect location, and aids in interference identification through waveform reconstruction [14]. Additionally, in the DGISC, the electric coupler shields the magnetic coupler against the power-frequency voltage. However, the combination of both sensors in the same mounting hole leads to undesirable interactions between them. The subsequent section outlines these interactions between the couplers and details the solutions adopted to minimise them.

3. Electric and magnetic sensors interaction

This section explores the interaction between both couplers within the same mounting hole without being connected to form a directional coupler. On one hand, the magnetic field coupled to the magnetic loop is reduced by the incorporation of the electric shield. On the other hand, the attachment of the electric coupler to the magnetic loop introduces an undesired resonance. To investigate these interactions, frequency-domain FEM simulations were conducted at 100 MHz, employing the electromagnetic wave equation (4). Here, μ_r represents the relative permeability, μ_0 and ε_0 denote the permeability and permittivity of free space, ω is the angular frequency, and $\hat{\varepsilon}$ represents the lossy permittivity (5). The first term in (5) is associated with the polarizability of the dielectric (ε_r), while the second is related to the conduction losses, where σ is the DC conductivity.

Moreover, frequency-domain measurements were performed in the TEM test bench illustrated in Fig. 4. A detailed description of the test bench can be found in [15]. In this setup, the input is connected to one of the transition cones, and the output signals are extracted from the sensors located at the mounting hole. The entire setup is tuned to 50 Ω, and the reflections can be controlled through the load at the output cone.

$$\nabla\times\frac{1}{\mu_r}(\nabla\times\boldsymbol{E})-\omega^2\varepsilon_0\mu_0\hat{\varepsilon}\boldsymbol{E}=0 \tag{4}$$

$$\hat{\varepsilon}=\varepsilon_r-\frac{j\sigma}{\omega\varepsilon_0} \tag{5}$$

Reference [5] demonstrated that the PD current generates a magnetic field in the xy-plane of the GIS mounting hole, illustrated in the coloured plane in Fig. 5 a). The time-varying magnetic field induces a voltage in the magnetic sensor, and any other conductor within the same xy-plane induces a counter-electromotive force in the magnetic coupler, reducing its sensitivity. Based on the TEM test bench, a FEM simulation was conducted to evaluate the capacitive and magnetic coupling of the electric and magnetic sensors, respectively. The electric sensor is mounted in between the high-voltage conductor and the magnetic loop, so the magnetic sensor does not interfere with the electric coupling. Therefore, to reduce the simulation time, the magnetic sensor was omitted. However, by knowing the magnetic flux in the magnetic sensor's plane ($\boldsymbol{\Phi}_z$), and the charge (Q) at the electric sensor's bottom face, their corresponding coupling inductance and capacitance can be approximated with (6).

$$M=\boldsymbol{\Phi}_z/\boldsymbol{I}_{pd}\ \text{and}\ C_1=Q/\left(\boldsymbol{I}_{pd}Z_{GIS}\right) \tag{6}$$

Fig. 5 b) shows the capacitance and inductance of the sensors concerning three variables: magnetic plane position (● [mm]), electric coupler diameter (O [mm]), and electric disk lossy permittivity (**X**). The magnetic plane position is measured from the GIS enclosure, aligning with the electric disk's top face (see Fig. 5a). For reference, the sensors' maximum capacitance (C_{max}) and inductance (M_{max}) were determined individually with a 98 mm diameter aluminium ($7x10^7$ S/m) disk, and a magnetic plane placed at $\mathbf{X}=2$ mm. These variables were independently simulated while keeping the remaining variables constant to the reference values, as shown in Table 1.

Results from varying the magnetic plane position indicate that the maximum magnetic flux no longer occurs at 2 mm due to the presence of the electric disk; instead, it shifts to 11 mm. Another approach to

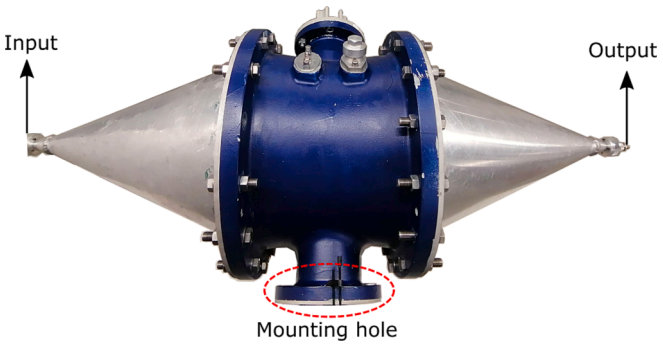

Fig. 4. Matched test bench used for sensors' characterisation.

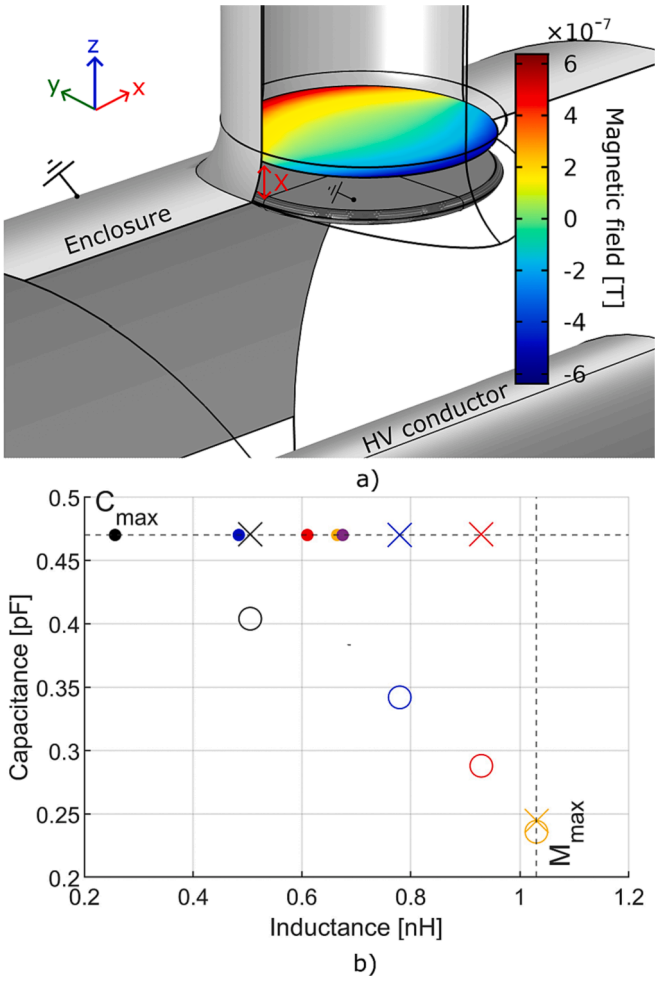

Fig. 5. A) finite element method simulation of the magnetic field induced in a xy-plane in the presence of an electric disk. b) capacitance and inductance simulation as a function of the parameters shown in Table 1.

Table 1
Parameters used for FEM simulation in Fig. 5.

	Magnetic plane position [mm]	Electric coupler diameter [mm]	Electric disk lossy permittivity
●	2	98	1E+10
●	5	98	1E+10
●	8	98	1E+10
●	11	98	1E+10
●	14	98	1E+10
O	2	94	1E+10
O	2	90	1E+10
O	2	86	1E+10
O	2	82	1E+10
×	2	98	1E+06
×	2	98	1E+04
×	2	98	1E+03
×	2	98	2E+00

diminish the electric disk magnetic coupling is by reducing the electric disk diameter. As depicted in Fig. 5 a), due to proximity effect, most of the magnetic field lies at the edge. Thus, by decreasing the electric disk diameter, the counter-electromotive force is diminished, reducing the electric coupling (C_1) as well. The third option involves increasing the disk impedance, revealing optimal electric and magnetic coupling with a lossy permittivity of 1×10^3. It is crucial to control this material permittivity to maintain the effectiveness of the power-frequency shield grading.

The material properties of the electric disk must fulfil the trade-off between shielding the 50 Hz power-frequency electric field and blocking the high-frequency Eddy currents. An electrostatic finite element simulation was conducted to determine the minimum required conductivity for an effective grading shield. The criterion involved reducing the shield's conductivity until the electric field at the magnetic loop exceeded the field when no loop was placed, resulting in a value of 4×10^{-7} S/m at 50 Hz. The material's lossy permittivity can be manipulated by incorporating carbon black into an epoxy resin mixture (CB). An Araldire® epoxy resin with 5% carbon black was cast, yielding a 100 MHz lossy permittivity of 20 and a 50 Hz conductivity of 1.7×10^{-5} S/m, as measured with the vector network analyzer.

Various parameters must be considered to achieve maximum gain with the two sensors. Fig. 6 shows the frequency response of the electric (a) and magnetic (b) couplers, both sharing the same mounting hole, with different disk configurations. The blue line represents a 100 mm diameter aluminium disk, matching the mounting hole's diameter, providing optimal electric coupling but with increased Eddy current. The red plot represents an aluminium disk reduced to 60 mm diameter, yielding a lower electric sensor's gain but without affecting the magnetic coupler. An alternative solution, plotted in black, is a 70 mm diameter aluminium disk with a 16 mm thick CB rim (Fig. 7). As demonstrated in Fig. 5, decreasing the material's permittivity at the disk's edge preserves the magnetic sensor's magnetic field. Furthermore, the incorporation of the aluminium disk into the CB rim allows better electric contact. Table 2 details the sensors' parameters calculated for the test bench. The described interaction between the electric and magnetic couplers arises from sharing the same mounting hole, even before interconnecting them to form a directional coupler.

4. Directional GIS coupler design

The electric connection of the electric and magnetic couplers can be conceptualized as a single sensor with an electric component (electric sensor's contribution) and a magnetic component (magnetic sensor's contribution). As shown in (3), to enhance the directional coupler's directivity, the magnetic and electric components must be similar to effectively segregate forward and backward pulses. Consequently, the

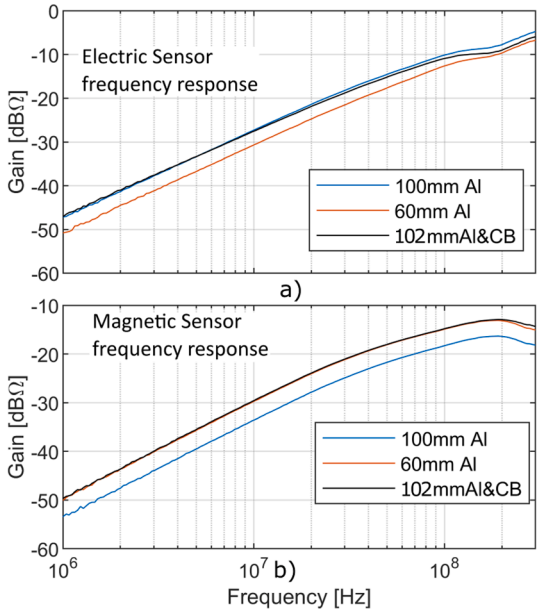

Fig. 6. A) electric and b) magnetic sensors' frequency response with different disk configurations[16].

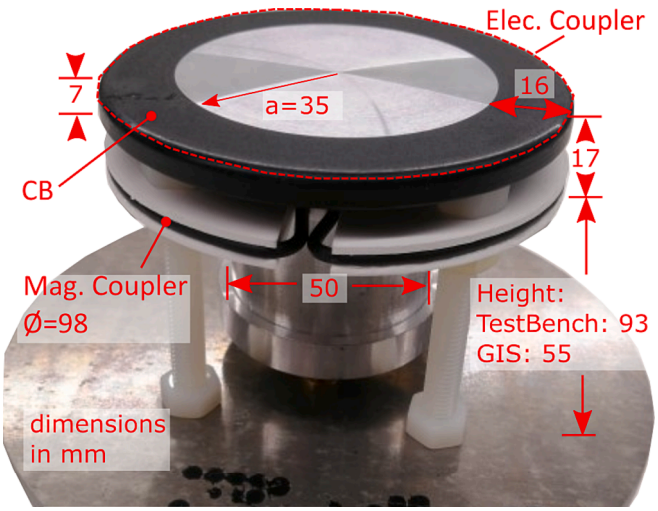

Fig. 7. Picture and dimensions of the electric and magnetic sensors in a single mounting hole configuration.

Table 2
Electric and magnetic sensors parameters with $R = Z_{GIS} = 50\ \Omega$.

	Electric parameters	Magnetic parameters
$k=$	$RZ_{GIS}C_1 \approx 0.75$ nΩs	$M \approx 0.6$ nΩs
$\omega_1=$	$1/C_2R \approx 6.7\text{x}10^8$ rad/s	$R/L_s \approx 3.7\text{x}10^8$ rad/s

design has to be tailored to align each component's zeros and poles. These parameters depend upon the sensor geometry subjected to the GIS mounting hole dimensions.

The electric and magnetic coupling constants (k) can be matched' by adjusting the electric and magnetic couplings (C_1 and M) with the parameters shown in Fig. 5. However, for the case of ω_1, adjusting the self-inductance (L) and the ground capacitance (C_2) proves challenging without influencing the other parameters. Fig. 3 shows that the currents originating from the electric coupler ($\boldsymbol{I}_e$) are common-mode, while the magnetic currents ($\boldsymbol{I}_m$) are differential-mode. Introducing a ferrite choke allows the adjustment of the electric's first pole without affecting other parameters. Fig. 8 depicts the induced impedance to a conductor coupled to the ferrite, reflected in the circuit as shown in Fig. 9, resulting in (7). Lastly, the second pole is typically above the frequency of interest, rendering it negligible and thus ignored.

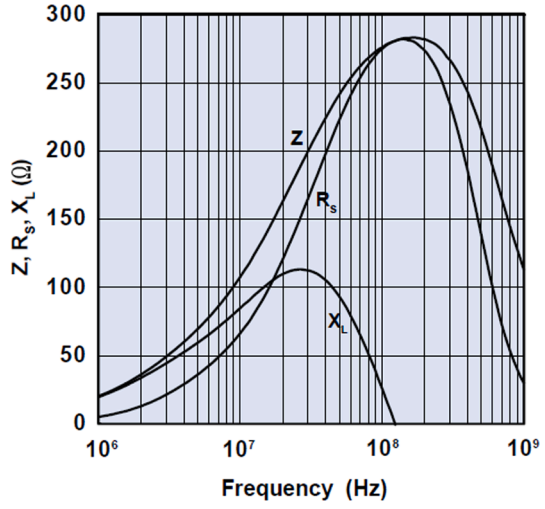

Fig. 8. Induced impedance in a cable coupled to a Fair-Rite 0443164251.

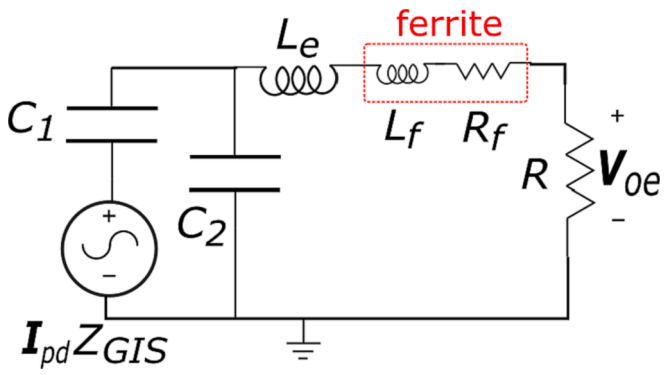

Fig. 9. Electric-component circuit with the ferrite choke.

$$\frac{\boldsymbol{V}_{oe}(s)}{\boldsymbol{I}_{pd}(s)} \approx \frac{sRZ_{GIS}C_1}{s^2\left(L_e + L_f(s)\right)C_2 + sC_2\left(R + R_f(s)\right) + 1} \tag{7}$$

The differential mode can be satisfied with a shielded magnetic loop probe, as demonstrated in [8] and [17]. The only accessible location for connecting the electric coupler to the shielded loop is at the gap. References [8] and [6] present diverse magnetic loop probes designed for GIS applications, including unshielded loops, unbalanced shielded loops, and balanced shielded loops, each featuring distinct gap configurations. Fig. 10 illustrates the electric coupler connected to both an unbalanced (bottom lobe) and a balanced (top lobe) loop. In the unbalanced configuration, nearly all the electric component's current (red arrows) flows through the grounded gap path. Conversely, in the balanced configuration, the electric component current encounters identical paths at the middle gap. Consequently, the self-inductance is reduced since the current flows evenly in each direction but with different polarities. Reference [17] shows the same effect for common-mode currents in magnetic probes for radio applications. The 8-shaped balanced magnetic loop, proposed in [18], doubles the magnetic coupler gain and allows the gap connection in the centre of the electric disk.

To evaluate the DGISC and assess the impact of the ferrite, measurements in the test bench were taken of the sensor's backward and forward outputs using the "8-shaped" balanced loop connected to a 90 mm diameter aluminium electric disk (Fig. 11). As previously mentioned, the forward output ($\boldsymbol{V}^+$) is the sum of both components, while the backward output ($\boldsymbol{V}^-$) is the difference between them, (8). Adding or subtracting these outputs allows the calculation of the electric (E_c) and the magnetic (M_c) components, as indicated in (9). Fig. 12 a) displays the outputs with and without ferrite chokes, demonstrating that

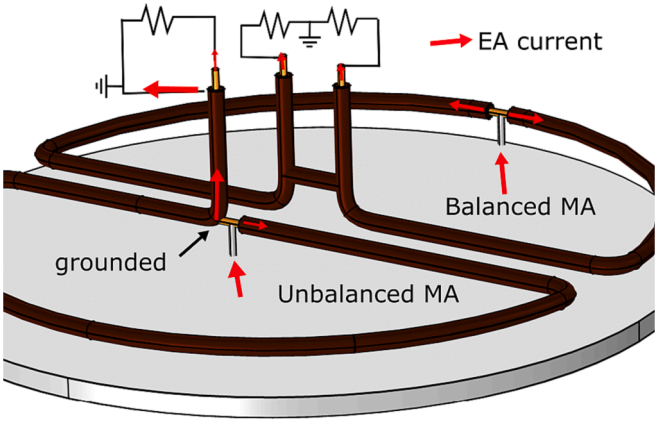

Fig. 10. Electric coupler's current distribution (red arrows) in an unbalanced loop (bottom lobe) and a balanced loop (top lobe).

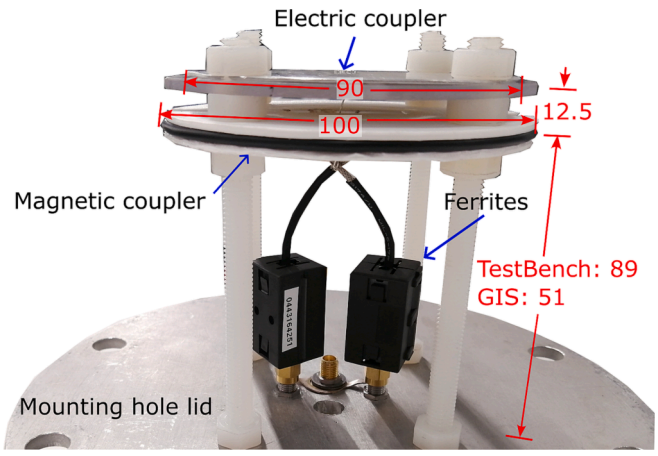

Fig. 11. Photo and dimensions of the DGISC.

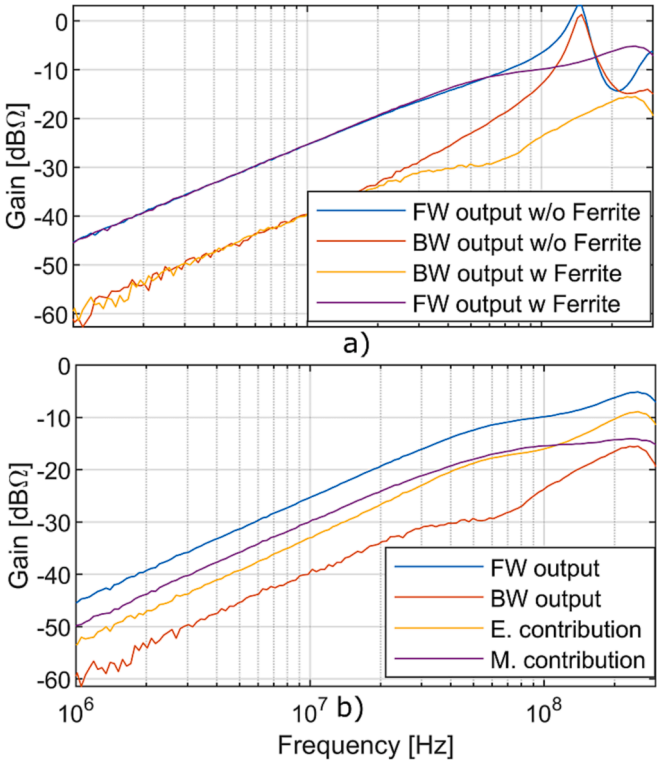

Fig. 12. A) forward and backward output frequency response with and without ferrite. b) forward and backward outputs' frequency response with ferrite choke, and calculated magnetic and electric contributions[16].

the ferrites shift the cutoff frequency and reduce the resonance peak. Fig. 12 b) illustrates both outputs with ferrite choke and the estimated electric and magnetic components using (9). Due to the inequality between the electric and magnetic elements, there is a 15 dB difference between the forward and backward outputs.

$$\boldsymbol{V}^{+} = E_c + M_c \text{ and } \boldsymbol{V}^{-} = E_c - M_c \tag{8}$$

$$E_c = (\boldsymbol{V}^{+} + \boldsymbol{V}^{-})/2 \text{ and } M_c = (\boldsymbol{V}^{+} - \boldsymbol{V}^{-})/2 \tag{9}$$

5. Calibration procedure

Reference [10] establishes that the PD charge (Q) can be estimated through the voltage double integral (V2I) method as expressed in (10), where V_o is the output voltage, t_0 is the pulse second zero-crossing, and k is the calibration constant. This calibration constant is the sensor's transfer function (G) slope when the frequency approaches zero, as shown in (11). The PD charge for the DGISC can be obtained using this procedure and the principle of superposition, where the charge estimation (Q_{DGISC}) is proportional to the addition of electric and magnetic constants, resulting in (12). The calibration constant can be obtained by measuring frequency response in the matched test bench.

$$Q \approx \frac{1}{k}\int_0^{t_0}\int_0^{t_0} V_o(t)dt \tag{10}$$

$$k \approx lim\left|\frac{G(\omega)}{\omega}\right|_{\omega\to 0} \quad when\ \omega \neq 0 \tag{11}$$

$$Q_{DGISC} \approx \frac{1}{k_e + k_m}\int_0^{t_0}\int_0^{t_0} V_o(t)dt \tag{12}$$

Fig. 13 depicts the calibration constant of the DGISC with its electric and magnetic contributions. The electric component (red) is obtained with an opened-circuited test bench, and the magnetic one (yellow) is extracted with a short-circuited test bench. The DGISC in the matched test bench is represented in blue. In the 1–10 MHz range, the calibration constant is 0.35 nΩs and 0.52 nΩs for the electric and magnetic contributions, respectively. Adding both components yields the same value as the DGISC's matched measurement of 0.87 nΩs. These results demonstrate that the calibration constant of the DGISC is equal to its electric and magnetic components' superposition.

While these measurements were conducted on the TEM test bench, determining the DGISC calibration constant directly in a full-scale GIS is challenging due to multiple discontinuities. Reference [6] outlines a method to find the electric and magnetic sensors' calibration constants in a full-scale GIS. The same approach can be applied to the DGISC, but it requires short-circuiting the GIS for the magnetic contribution, and open-circuiting it for the electric one.

6. Pulse reflectometry and charge estimation

The directional GIS coupler's directivity and charge estimation were tested both in the TEM test bench and a full-scale GIS. The DGISC is compared against the software synergy using the magnetic and electric couplers from Fig. 7.

6.1. Matched test bench

In the matched test bench, the input pulse and discontinuities are controllable, providing less uncertainty compared to the full-scale GIS. Two scenarios were examined: a discontinuity positioned far from the

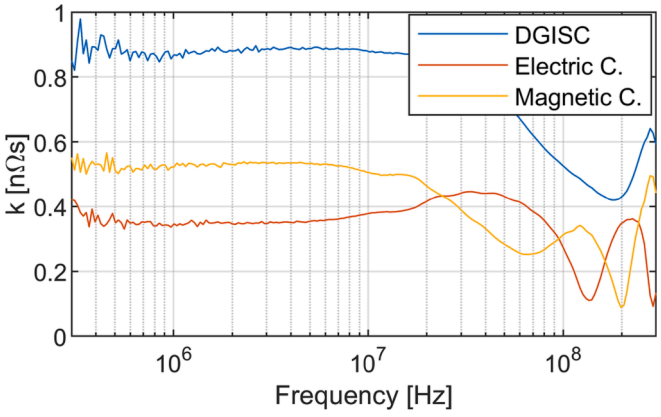

Fig. 13. Calibration constant of the DGISC and electric and magnetic contributions [16].

sensors without pulse overlapping and a discontinuity placed close to the sensors with pulse overlapping. Utilizing the test setup illustrated in Fig. 4, a UHF pulse was applied to the input cone, and the discontinuities were introduced in the output cone. The sensors parameters for the software synergy and the DGISC are provided in Table 2 and Fig. 13, respectively.

When a discontinuity is sufficiently distant from the sensor, the reflected pulse experiences a noticeable delay from the incident pulse. Fig. 14 illustrates the DGISC's forward and backward measurements when the test bench is open-circuited at 520 cm from the sensors. In plots a) and b), the outputs are filtered with 190 MHz and 98 MHz low-pass filters (LPF), resulting in a charge estimation error of 16% and 3%, respectively (Table 3). Improved reflection suppression and charge estimation were achieved with the 98 MHz LPF filter, as the electric and magnetic sensors' transfer functions exhibit greater similarity at lower frequencies.

When the discontinuity is close to the sensor's location, the incident and reflected pulses overlap, distorting the measured pulse. Fig. 15 compares pulses without overlapping against those with overlap when the discontinuity is positioned 76 cm away. In Fig. 15 a), the electric and magnetic couplers' measurements are presented for both matched ("M" in the figure legend) and unmatched ("UM" in the figure legend) conditions. The forward and backward measurements from the software synergy and the DGISC are illustrated in Fig. 15 b) and c), respectively. In both sensors, the incident pulse is effectively segregated, exhibiting a similar shape to the matched measurement. Table 3 shows the charge estimation for the directional GIS coupler and the software synergy. The DGISC, when utilizing the 98 MHz LPF, gave a 0.3% charge estimation error, representing the best estimation. The low errors with the DGISC can be attributed to the zero-time delay difference between the electric and magnetic contribution. In contrast, the software synergy requires the calculation of the time delay between the electric and magnetic sensors.

6.2. Full-scale GIS

This section shows the software synergy and the DGISC in a full-scale gas-insulated substation. The GIS is depicted in Fig. 16 a), with PDs generated at the end of the GIS. The sensors were positioned 94 cm away from the T-branch. A propagated pulse in the TEM mode frequency perceives the T-branch as a discontinuity with half the characteristic impedance, reflecting part of the pulse [19]. The test setup is illustrated in Fig. 16 b), where two PD sources in SF_6 test cells were tested: a jumping particle (JP) defect at 4.5 $bars_{abs}$ and a surface discharge (SD) at 3 $bars_{abs}$. The test cells' electrodes were connected to the GIS' high-voltage conductor and the enclosure through a rod, with a high-frequency current transformer (HFCT) coupled to the rod. The HFCT served as a reference for PD charge estimation, with a 4 kHz-1 GHz bandwidth. The sensors were connected to a 31.5 dB, 1 GHz voltage amplifier, followed by low-pass filters. For safety reasons, surge arresters with 100 MHz cutoff frequency were connected in parallel to the oscilloscope input. The HFCT's broadband response enabled the calculation of the reference charge using the pulse current integration method [20]. Table 4 presents the couplers' calibration constants and the first poles used for the software synergy method. Due to the full-scale GIS mounting hole's geometry, the sensors' parameters gave different values than the matched test bench.

The charges of 200 PDs were estimated for two defects: jumping particle and surface discharge. In accordance to the IEC standard [22] and CIGRE [23], the maximum allowed PD charge value in a new GIS is 5 pC, and any PD measuring system is expected to sense at least this magnitude. Therefore, SD with a charge magnitude in the order of 5 pC were measured. Table 5 displays the mean and standard deviation errors using different filters and sensors. These errors have a systematic and random component, as shown in [21]. The standard deviation comes from the random noise, which is more pronounced for lower-magnitude signals. Conversely, the systematic error is attributed to the charge estimation method, the calibration constant estimation, and overlapping

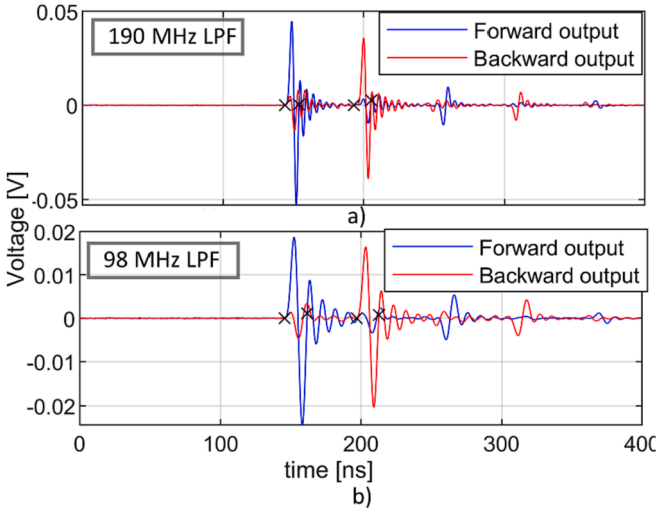

Fig. 14. Measured incident and reflected pulse with a discontinuity 520 cm away from DGISC a) using a 190 MHz LPF and b) using 98 MHz LPF. The charge estimation zero-crossings are marked with an "x" [16].

Table 3
Charge estimation using software synergy and DGISC with 520 cm and 76 cm discontinuity.

Discontinuity distance	LPF	Software synergy	DGISC
520 cm	190 MHz	13 %	16 %
520 cm	98 MHz	22 %	3 %
76 cm	98 MHz	23 %	0.3 %

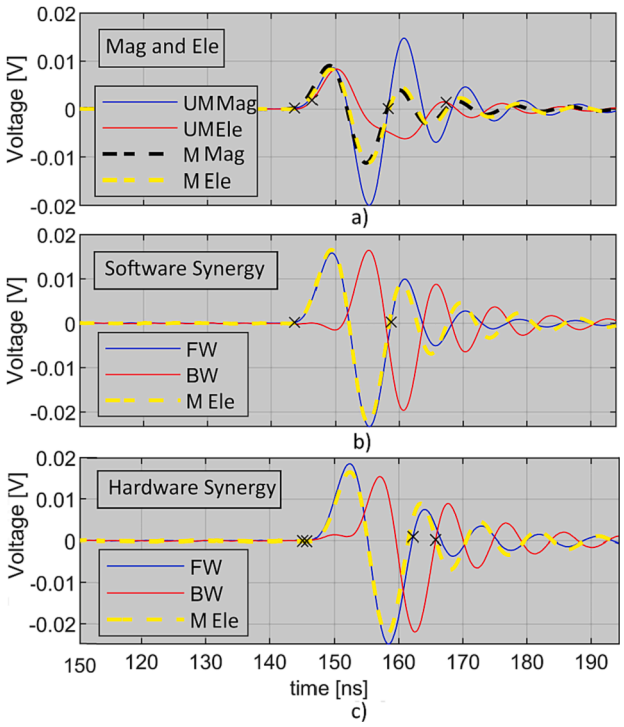

Fig. 15. Comparison of matched pulses (M) and unmatched pulses (UM), using a) magnetic (Mag) and electric (Ele) sensors, b) software synergy's forward (FW) and backward (BW) components, and c) DGISC forward and backward components. The charge estimation zero-crossings are marked with an X [16].

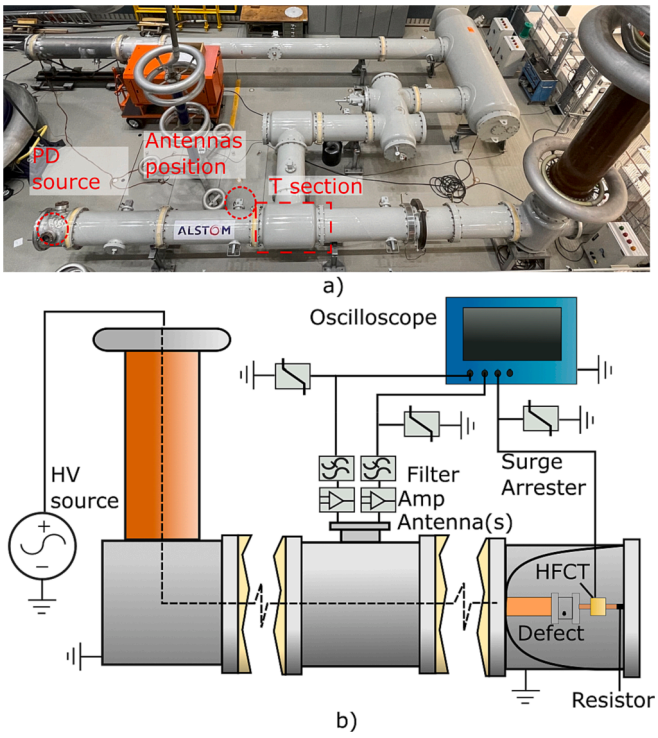

Fig. 16. A) full-scale GIS picture indicating the PD source, sensors, and t-section. b) full-scale GIS test setup for measuring PD.

Table 4
Parameters of the electric couplers (EC), magnetic couplers (MC) and DGISC in the full-scale GIS.

	EC	MC	DGISC
k [nΩs]	2.5	0.68	1.7
ω_0 [rad/s]	$5.7\text{x}10^8$	$3.1\text{x}10^8$	NA

Table 5
Charge estimation error with different defects, LPFs, and sensors [16].

	Mean ± Standard deviation error [%]			
LPF [MHz] @defect	Magnetic sensor	Electric sensor	Software Synergy	DGISC
48 @JP	51 ± 9%	−32 ± 4%	3 ± 5%	9 ± 4%
98 @JP	28 ± 5%	−22 ± 3%	−5 ± 3%	25 ± 8%
190 @JP	21 ± 7%	−20 ± 6%	−9 ± 6%	25 ± 8%
48 @SD	48 ± 25%	−41 ± 6%	−6 ± 12%	−10 ± 13%
98 @SD	−4 ± 7%	−40 ± 3%	−29 ± 5%	−21 ± 5%
190 @SD	−15 ± 4%	−41 ± 3%	−35 ± 4%	−21 ± 7%

of reflected pulses, where the last two are exclusive to this test setup.

The change of impedance at the T-branch overlaps the incident pulse constructively for the magnetic measurements (overestimation) and destructively for the electric sensor (underestimation). This phenomenon can be seen in Table 5: as the filtered frequency decreases, the pulse duration increases, leading to overlapping. The software synergy significantly reduces charge estimation errors by mitigating reflection overlaps. Fig. 17 compares the reference charge against the couplers and the software synergy filtered at 48 MHz: the magnetic coupler's charges are overestimated, and the electric coupler's ones are underestimated. For the DGISC, the best charge estimation is achieved when filtered at 48 MHz because the electric and magnetic contributions are more

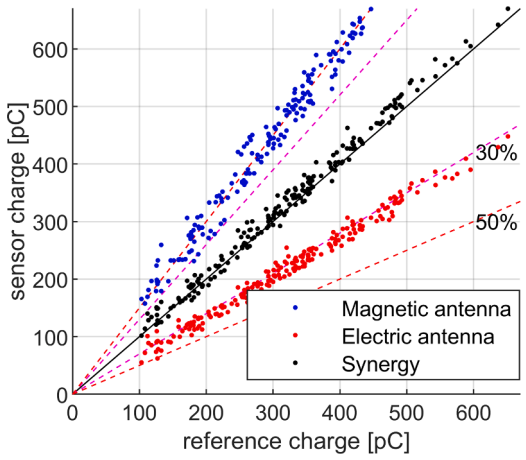

Fig. 17. Charge estimation of jumping particle PD using magnetic and electric sensors and software synergy filtered at 48 MHz [16].

similar at lower frequencies. Fig. 18 compares the reference charge against the DGISC filtered at 48 MHz. As expected, the forward values show a higher magnitude than the backward output, as the former is calculated for the incident pulse and the latter for the attenuated reflected pulse.

7. Conclusions

In GIS PD measurements, multiple discontinuities distort the wave shape and PD charge estimation. The forward and backward components can be measured with electric and magnetic sensors placed in the same GIS longitudinal position. In most cases, the mounting holes are already used for different purposes, making it convenient to place the PD sensors in a single one. This paper addressed the challenges of electric and magnetic couplers sharing the same mounting hole, creating a high-voltage directional coupler. The following conclusions were drawn from this research:

- The interactions between the electric and the magnetic couplers were addressed using a carbon-black-epoxy electric coupler.

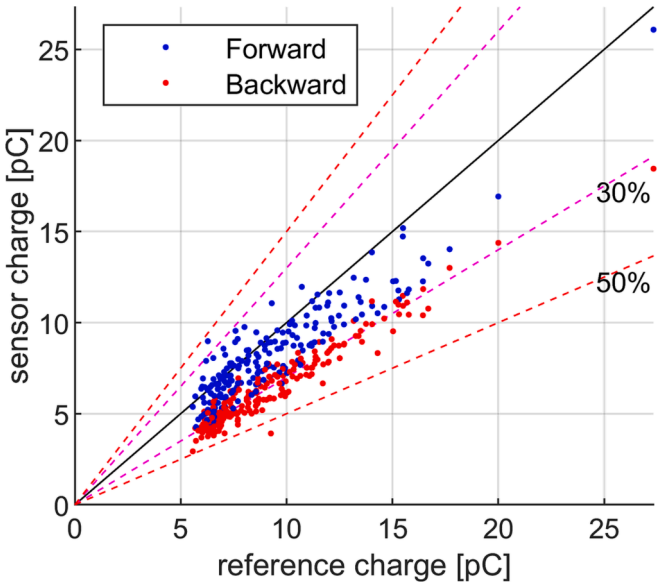

Fig. 18. DGISC filtered at 48 MHz vs. reference charge for a surface discharge defect [16].

- Ferrite chokes can be used to adjust the sensor's transfer function for better directional coupler directivity.
- The DGISC yielded satisfactory results distinguishing between PD's forward and backward components up to 50 MHz, improving the PD charge estimation.
- The DGISC directivity bandwidth is limited by the matching of the electric and magnetic sensors' parameters.
- The DGISC is capable of discern forward and backward components with a better performance at low frequency.
- The DGISC showed better charge estimation than the independent couplers for a bandwidth up to 48 MHz.

The next steps involve creating an optimized design to improve the sensors' directivity and bandwidth. This study represents a step forward in online PD monitoring and PD charge estimation in modern GIS with SF_6-alternative gases.

CRediT authorship contribution statement

Christian Mier: Conceptualization, Methodology, Formal analysis, Investigation, Writing – original draft, Visualization, Writing – review & editing. **Armando Rodrigo Mor:** Conceptualization, Writing – review & editing, Supervision, Project administration. **Peter Vaessen:** Writing – review & editing, Project administration.

Declaration of Competing Interest

The authors declare that they have no known competing financial interests or personal relationships that could have appeared to influence the work reported in this paper.

Data availability

The data was submitted to "Mendeley Data" repositorium and it is cited in the article in the corresponding figures.

Acknowledgements

This project 19ENG02 FutureEnergy has received funding from the EMPIR programme co-financed by the Participating States and from the European Union's Horizon 2020 research and innovation programme. Funder ID: 10.13039/100014132.

Declaration of Generative AI and AI-assisted technologies in the writing process

During the preparation of this work the authors used ChatGPT in order to improve the readability and language of this article. After using these tool/service, the authors reviewed and edited the content as needed and take full responsibility for the content of the publication.

References

[1] A. Cavallini, G.C. Montanari, M. Tozzi, PD apparent charge estimation and calibration: A critical review, IEEE Trans. Dielectr. Electr. Insul. 17 (1) (2010) 198–205, https://doi.org/10.1109/TDEI.2010.5412018.
[2] IEC 60270, Partial Discharge Measurements, 2015.
[3] H. Okubo, N. Hayakawa, A. Matsushita, The relationship between partial discharge current pulse waveforms and physical mechanisms, IEEE Electr. Insul. Mag. 18 (3) (2002) 38–45, https://doi.org/10.1109/MEI.2002.1014966.
[4] G. Behrmann, S. Franz, J. Smajic, Z. Tanasic, R. Christen, UHF PD signal transmission in GIS: Effects of 90° bends and an L-shaped CIGRE step 1 test section, IEEE Trans. Dielectr. Electr. Insul. 26 (4) (2019) 1293–1300, https://doi.org/10.1109/TDEI.2019.008005.
[5] A. Rodrigo-Morz, F. A. Muñoz, L.C. Castro-Heredia, A novel antenna for partial discharge measurements in GIS based on magnetic field detection, Sensors (Switzerland), vol. 19, no. 4, 2019, doi: 10.3390/s19040858.
[6] C. Mier, A. Rodrigo Mor, L. Castro, P. Vaessen, Magnetic and electric antennas calibration for partial discharge charge estimation in gas-insulated substations, Int. J. Electr. Power Energy Syst. 141 (January) (2022), 108226, https://doi.org/10.1016/j.ijepes.2022.108226.
[7] S. Ohtsuka, T. Teshima, S. Matsumoto, M. Hikita, Relationship between PD induced electromagnetic wave measured with UHF method and charge quantity obtained by PD current waveform in model GIS, Electrical Insulation and Dielectric Phenomena (2006) 615–618, https://doi.org/10.1109/CEIDP.2006.312007.
[8] C. Mier, A.R. Mor, P. Vaessen, Design and Characterization of a Magnetic Loop Antenna for Partial Discharge Measurements in Gas Insulated Substations, IEEE Sens. J. 21 (17) (2021) 18618–18625, https://doi.org/10.1109/JSEN.2021.3089084.
[9] R. Kurrer, Teilentladungsmessung im Gigaherts-Frequencbereich an SF6-isolierten Schaltanlagen, Stuttgart (1997).
[10] A. Rodrigo-Mor, F.A. Muñoz, L.C. Castro-Heredia, Principles of charge estimation methods using high-frequency current transformer sensors in partial discharge measurements, Sensors (Switzerland), vol. 20, no. 9, 2020, doi: 10.3390/s20092520.
[11] H. Imagawa, K. Emoto, H. Murase, H. Koyama, R. Tsuge, S. Maruyama, T. Sakakibara, PD signal propagation characteristics in GIS and its location system by frequency components comparison, IEEE Trans. Power Deliv. 16 (4) (2001) 564–570.
[12] C. Mier, A. Rodrigo Mor, P. Vaessen, A. Lathouwers, Magnetic and electric antennas synergy for partial discharge measurements in gas-insulated substations: Power flow and reflection suppression, Int. J. Electr. Power Energy Syst. 144 (January) (2023) 1–9, https://doi.org/10.1016/j.ijepes.2022.108530.
[13] S.M. Mousavi, S.A. Mirtaheri, M.A. Khosravani-Moghaddam, B. Habibi, J.S. Meiguni, Design, fabrication and test of a broadband high directivity directional coupler, ICEE 2015 - Proc. 23rd Iran. Conf. Electr. Eng., vol. 10, pp. 168–170, 2015, doi: 10.1109/IranianCEE.2015.7146203.
[14] F. Alvarez, J. Ortego, F. Garnacho, M.A. Sanchez-Uran, A clustering technique for partial discharge and noise sources identification in power cables by means of waveform parameters, IEEE Trans. Dielectr. Electr. Insul. 23 (1) (Feb. 2016) 469–481, https://doi.org/10.1109/TDEI.2015.005037.
[15] C. Mier, A.R. Mor, Test Bench and Frequency Response of a Magnetic Antenna used in GIS PD Measurements, no. 2, pp. 269–272, 2021, doi: 10.1109/eic49891.2021.9612372.
[16] C. Mier, GISDicCoup, Mendeley Data 1 (2022), https://doi.org/10.17632/dfr5h8rhns.1.
[17] C.F.M. Carobbi, L.M. Millanta, Analysis of the Common-Mode Rejection in the Measurement and Generation of Magnetic Fields Using Loop Probes, IEEE Trans. Instrum. Meas. 53 (2) (2004) 514–523, https://doi.org/10.1109/TIM.2004.823297.
[18] C.M. Escurra, A.R. Mor, Balanced Magnetic Antenna for Partial Discharge Measurements in Gas-Insulated Substations, in: in 2022 9th International Conference on Condition Monitoring and Diagnosis, CMD 2022, 2022, pp. 509–512, https://doi.org/10.23919/CMD54214.2022.9991698.
[19] W. Gao, D. Ding, D. Zhao, W. Liu, Propagation properties of high-frequency electromagnetic wave through typical in-field GIS structures, IEEE Trans. Power Deliv. 29 (6) (2014) 2476–2484, https://doi.org/10.1109/TPWRD.2014.2356500.
[20] A.R. Mor, P.H.F. Morshuis, J.J. Smit, Comparison of charge estimation methods in partial discharge cable measurements, IEEE Trans. Dielectr. Electr. Insul. 22 (2) (2015) 657–664, https://doi.org/10.1109/TDEI.2015.7076760.
[21] C. Mier Escurra, A. Khamlichi, M. Dalstein, J. Ramón Vidal, F. Garnacho, A. Rodrigo Mor, T. Vu-Cong, Methods for Partial Discharge Calibration in Gas-Insulated Substations for HVDC Power Grids and Charge Evaluation Uncertainty, IEEE Sens. J. 23 (19) (2023) 23486–23493.
[22] International, Electrotechnical, and COMMISSION, IEC 62271: High-voltage switchgear and controlgear – Part 203: AC gas-insulated metal-enclosed switchgear for rated voltages above 52 kV, vol. 3. 2022.
[23] C. W. 33/23.12, Insulation Co-ordination of GIS: return of experience, on site tests and diagnostic techniques, Electra, vol. 176, pp. 67–97, 1998.